electronics

MDPI

Article

A New Decentralized PQ Control for Parallel Inverters in Grid-Tied Microgrids Propelled by SMC-Based Buck–Boost Converters

Ali M. Jasim [1,2,*], Basil H. Jasim [1] and Bogdan-Constantin Neagu [3,*]

[1] Electrical Engineering Department, University of Basrah, Basrah 61001, Iraq
[2] Department of Communications Engineering, Iraq University College, Basrah 61001, Iraq
[3] Power Engineering Department, Gheorghe Asachi Technical University of Iasi, 700050 Iasi, Romania
* Correspondence: e.alim.j.92@gmail.com (A.M.J.); bogdan.neagu@tuiasi.ro (B.-C.N.)

Abstract: Nowadays, the microgrid (MG) concept is regarded as an efficient approach to incorporating renewable generation resources into distribution networks. However, managing power flows to distribute load power among distribution generators (DGs) remains a critical focus, particularly during peak demand. The purpose of this paper is to control the adopted grid-tied MG performance and manage the power flow from/to the parallel DGs and the main grid using discrete-time active/reactive power (PQ) control based on digital proportional resonant (PR) controllers. The PR controller is used to eliminate harmonics by acting as a digital infinite-impulse response (IIR) filter with a high gain at the resonant frequency. Additionally, the applied PR controller has fast reference signal tracking, responsiveness to grid frequency drift, and no steady-state error. Moreover, this paper describes the application of robust nonlinear sliding mode control (SMC)-technique-based buck–boost (BB) converters. The sliding adaptive control scheme is applied to prevent the output voltage error that occurs during DG failure, load variations, or system parameter changes. This paper deals with two distinct case studies. The first one focuses on applying the proposed control for two parallel DGs with and without load-changing conditions. In the latter case, the MG is expanded to include five DGs (with and without DG failure). The proposed control technique has been compared with the droop control and model predictive control (MPC) techniques. As demonstrated by the simulation results in MATLAB software, the proposed method outperformed the others in terms of both performance analysis and the ability to properly share power between parallel DGs and the utility grid.

Keywords: microgrids; PQ control; digital PR control; sliding mode control; parallel inverters; model predictive control; distributed renewable resources

Citation: Jasim, A.M.; Jasim, B.H.; Neagu, B.-C. A New Decentralized PQ Control for Parallel Inverters in Grid-Tied Microgrids Propelled by SMC-Based Buck–Boost Converters. *Electronics* **2022**, *11*, 3917. https://doi.org/10.3390/electronics11233917

Academic Editor: Jesus C. Hernandez

Received: 10 October 2022
Accepted: 25 November 2022
Published: 27 November 2022

1. Introduction

The widespread use of fossil fuel, which may be exhausted by the end of the century, has been linked to a host of problems, including low air quality indices, environmental pollution, and a slew of others. In order to combat this, renewable, environmentally friendly clean energy is used and converted into electrical energy, which not only increases the diversity of energy usage but also reduces the consumption of fossil fuels for power-generating reasons. This energy comes from a variety of long-term sources such as solar, wind, and other distribution energy resources (DERs), all of which are being increasingly adopted to build microgrid (MG) resources. Power electronics converters are used to connect most DERs to the grid because of their controllability, flexibility, and monitoring capabilities [1–3].

In a variety of grid-related and industrial applications, DC/DC converters are used a lot to efficiently convert an unregulated voltage from the DERs to a regular one at the desired level to supply the inverters and operate DC loads in MGs. DC/DC power converters (buck, boost, and buck–boost) are the three primary types of DC/DC converters. They

can be controlled in a variety of ways, beginning with complete linear control techniques such as hysteretic, pulse width modulation (PWM) and progressing to nonlinear control techniques such as SMC. Due to its robustness against disturbances and uncertainties, the SMC technique has overcome the limitations of previous methods, and it has been adopted in the proposed control technique of the MG in this paper [4].

One of the most pressing issues in MG research is how to design controllers that ensure the MG operates reliably and stably in both grid-isolated and grid-connected modes. Specifically, it is necessary to control the frequency and voltage of each power electronic converter connected to each DG in the islanded mode, referred to as VF control, whereas it is necessary to regulate the output active and reactive powers of each DG in the grid-connected mode, referred to as PQ control. MGs are incorporated into the main grid while operating in the grid-tied mode to inject electricity into the utility grid. In order for the MG to function properly, the frequency and voltage of the main grid must be maintained [5–7]. Additionally, a solution to the power-sharing issue and meeting the load demand are the second challenges that necessitate the implementation of certain high-level solutions. In order to meet the anticipated power demand, the DGs are expected to distribute energy according to a predetermined power-sharing base. As explained in [8,9], the energy capacities of individual DGs can be represented by power-sharing bases. The challenge of power sharing has steadily risen to the top of the list of researcher priorities. For a long period of time, advanced control strategies for inverters have been investigated in power electronics topics. Additionally, with the growing number of inverter-connected DERs in modern, high-tech power grids, inverter control is critical to achieving improved DER performance. These DERs are connected to the MG's shared AC bus in parallel. Therefore, an analysis of power systems with parallel inverters is essential for enhancing power quality and keeping the grid stable [10]. Studies have investigated multiple contributions to the parallel configuration of grid-connected inverters [11–13]. In addition, many different strategies for controlling grid-connected inverters have been studied with the goal of making power systems more efficient. From the perspective of DERs, inverters should be monitored so that they can supply actual power to meet demand and export any excess to the grid. Interfaces' ability to supply reactive power to the grid would boost its power quality and reliability. Therefore, cutting-edge methods of DER control for optimizing power flow are to be anticipated [14]. Many state-of-the-art manufacturing controls [15] use model predictive control (MPC) algorithms. There are two types of MPC techniques used with inverters: (a) the finite control set MPC (FCS-MPC) approach, which uses the limited number of switching possibilities offered by the converter to address optimization problems, and (b) the continuous control set MPC (CCS-MPC) approach, which calls for a modulator to produce switching states from the controller. The FCS-MPC has a natural and efficient algorithm for controlling power converters without the use of PI controllers and modulators [16]. To regulate parallel inverters in numerous contexts, including DGs and MGs, the conventional droop control method is a commonplace control scheme. This unique method of control involves monitoring the system's reference points, measuring active and reactive powers, and adjusting the terminal voltage magnitude of each inverter locally and proportionally. Droop control methods have the inherent weakness of a slow transient response [17] due to the computation of instantaneous power and the low pass filter constraint. Additionally, numerous PQ control techniques can be used for integrating inverter-based DGs with the power system, including hysteresis, dead-beat (DB) controllers, proportional integral (PI) controllers, and PR controllers [18–21]. While hysteresis control is easy and responsive, the output current contains large ripples, resulting in poor current quality and making the output filter design more challenging [18]. Because it performs well with current-controlled DGs, DB predictive control is commonly employed. It is, nevertheless, exceedingly intricate and highly dependent on system settings [19]. If the objective is to correct the many harmonics behind sinusoidal signals and reduce steady-state error, the PR control technique in the synchronous reference frame is popular, while PI controllers provide more steady-

state error and are cohesive with the parameter setting problem [20]. To ensure optimal performance, however, the resonant frequency and changing grid frequency should be equal [21]. Typically, PQ controllers employ double-loop controls [22]. The outer power loop generates the reference current based on the power target, while the current inner loop serves as a fine-tuning circuit [22]. To the authors' knowledge, the literature focuses mostly on single-inverter systems, with only a few references devoted to parallel grid-tied inverters that do not use fully digital PR controllers based on PQ control. In this context, Bayo-Salas et al. [23] conducted a stability investigation of control interactions in a two-parallel-inverters system. Li et al. [24] presented a control strategy for an AC-grid-based multi-infeed inverter. Kammer et al. [25] introduced a frequency-domain current control technique for parallel grid-connected inverters. A significant disadvantage of these techniques is that the control design is reliant on the system's global model. As a result, conventional control systems cannot ensure the stability of the entire grid in the event of a grid configuration change (e.g., when the inverter is disconnected). In a rotating reference frame, the authors of [26] proposed a scalable control technique based on dq-currents for parallel inverters. A decentralized multivariable PI current control method underpins the control framework. Using a second-order generalized integrator, the research in [27] examined the active and reactive power control problem in a grid-connected single-phase fuel cell system using a boost inverter (the boost inverter was comprised of two bidirectional boost converters with their respective outputs connected in series).The authors of [28] suggested a PQ control approach for solar photovoltaics with maximum power point tracking, also known as MPPT, and battery storage while connected to the grid. A PQ control strategy for regulating the power produced by solar PVs and battery storage was presented [29]. Reference [30] focused on a method for two parallel inverters in microgrids to control power flow predictively. The microgrid in this case study was grid-tied, with an appropriate capacity for power sharing between parallel distributed generation and the main grid. Yixin Zhu et al. [31] proposed a precise technique for power sharing, relying on a communication platform and a droop control mechanism. The MG control center (MGCC) receives reactive power commands from the DG units and uploads information about power output. Active power sharing, in this case, may lead to inefficient reactive power flows between DG units. The voltages of such buses, connecting to the loads, fluctuate in response to changes in the active component of the current consumed by the loads, but because reactive power is not shared, the grid becomes unstable [32]. To achieve successful reactive power sharing, methods based on droop control approaches are adopted, such as enhanced droop control methods. They have high reliability but require a sophisticated algorithm, are inappropriate for complex microgrids, and have high communication line latency [33].

According to the authors' knowledge, no prior research has addressed the control of parallel inverters utilizing decentralized digital processing propelled by SMC-based BB converters. This paper proposes a new discrete PQ control technique based on PR controllers for grid-connected parallel DGs that utilize synchronous reference frames to improve power flow transients, eliminate steady-state errors, and offer a quick transient response. The following are the highlight points of the paper's contributions:

1. The proposed control-technique-based parallel DGs are completely decentralized. It is necessary that each DG be aware of its own power-sharing basis, which enables the proposed method to function as a plug-and-play solution due to its plug-and-play capacity.
2. This paper proposes a robust discrete-time PQ control structure by designing digital PR controllers for the power and current control loops of each DG to improve the accuracy and load-sharing capability of the parallel inverters operating in an MG framework.
3. Parallel decentralized mode SMC-based BB converters have been adopted to avoid voltage error and provide stable DC voltages for the related parallel inverters. SMC enables the controlled converters to operate flawlessly in high-signal operating conditions, allowing them to maintain efficient regulation and dynamic performance even when there are significant changes in the line, load, and system parameters.

4. The design process for digital power and current PR controller-based inverters is discussed in this paper. The procedure explains how to calculate resonant and proportional gains, as well as the resonant path coefficients, step by step. Its main contribution is to make researchers' jobs easier by facilitating and assisting them in developing inverters that incorporate existing control strategies in a digital environment. A frequency-domain analysis of a digital PR controller will also be presented in the paper. A fictitious w-domain was used in this study. The inverter's efficacy was demonstrated in the case study when it was used in conjunction with digital PR power and current controllers designed using the proposed procedure.
5. The proposed technique is compared to MPC and droop control techniques. The proposed technique outperforms the other techniques in terms of overall power flow control performance.

Regarding the remainder of this paper, its format is as follows. In Section 2, we describe a grid-tied parallel DG system. In the following section, we illustrate load-sharing power flow control. Information regarding the proposed control technique is provided in Section 4. Section 5 discusses power control based on MPC. In Section 6, we conduct extensive simulation studies to analyze the effectiveness of the proposed controller. Section 7 is the conclusion of the paper.

2. Grid-Tied Parallel DG System

Once the MG is connected to the main grid, the DGs provide the necessary power to the loads in conjunction with the grid, allowing the MG to become self-sufficient. If the generated power from DGs is less than the power required by the load, the grid will inject the additional power required by the load. In contrast, if the power from the DGs is more than the load requirements, the surplus energy will be returned to the grid. Multiple grid-tied inverters can be connected in parallel to the grid so that the combined currents from the grid and the loads are equal to the total current through the PCC of all the inverters. This occurs in MGs when multiple DERs are connected to the utility grid by way of a shared AC bus, as shown in Figure 1. Two parallel grid-tied DGs are used in the first case study of the system topology in this paper. Each DG is equipped with a three-phase two-level voltage source inverter (VSI) and a buck–boost DC/DC converter. The DC inverter input (V_{dc}) can be supplied from the SMC-based BB converter.

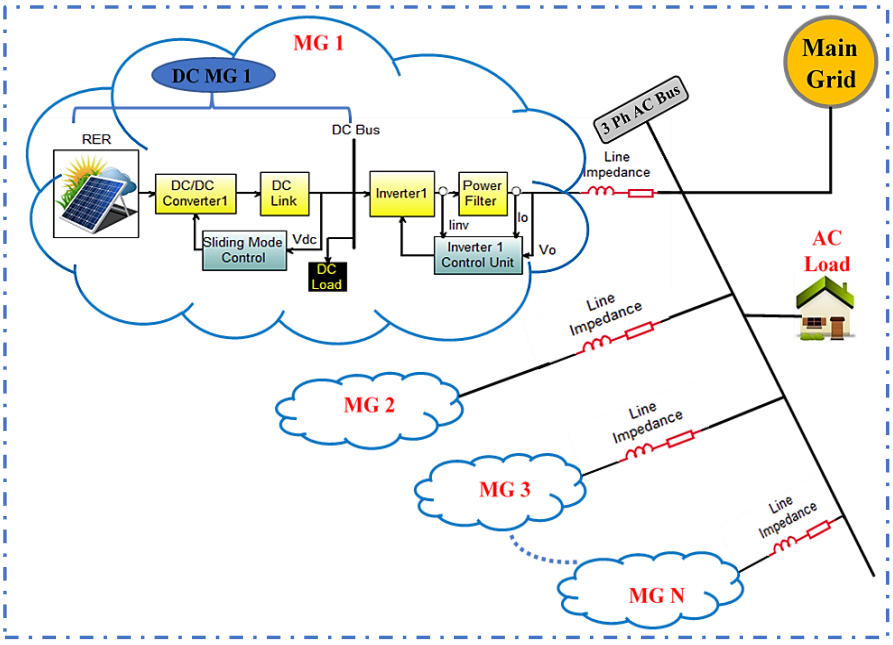

Figure 1. Parallel decentralized MGs.

The grid-tied inverter's topology is comprised of three complementary pairs of IGBT power switches. For an ***n***-phase ***i***-level converter, the total number of possible switching states is defined as $k = n^i$. Thus, eight possible switching states for a VSI can be identified. Figure 2 shows the voltage vectors generated by each inverter, which are composed of six active voltage vectors (numbered 1 through 6) and two zero voltage vectors (numbered 0 and 7). The VSI's eight voltage vectors are denoted by [30],

$$v_k = \begin{cases} \frac{2V_{dc}}{3} e^{j(k-1)\frac{\pi}{3}} & k = 1, \ldots, 6. \\ 0 & k = 0, 7 \end{cases} \quad (1)$$

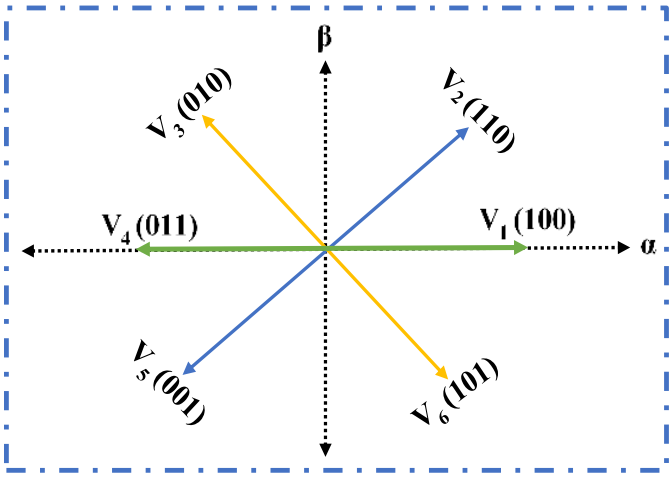

Figure 2. Three-phase two-level inverter output voltage vectors.

3. Load-Sharing Power Flow Control

The complicated power flow, denoted by [30,34], $S_k = P_k + Q_k$, between the common AC bus and the DGs, is represented by

$$P_k = \frac{|V_k|(|V_k|\cos\delta_k - |E|\cos(\delta_k + \theta_z))}{|z|} \; k = 1, 2 \quad (2)$$

$$Q_k = \frac{|V_k|(|V_k|\sin\delta_k - |E|\sin(\delta_k + \theta_z))}{|z|} \; k = 1, 2 \quad (3)$$

where V_k and E are the voltage vectors of the k-th inverter output and the common AC bus, $Z = R + jX = |z|\angle\theta_z$ is the line impedance, and $\delta_k = \theta_{zk} - \theta_E$ is the power angle. The line resistance is usually small and can be ignored, so the line impedance is $Z = jX = |z|\angle\, 90°$.

Due to the fact that δ_i is typically small, we can assume $\sin(\delta_k) = \delta_k$ and $\cos(\delta_k) = 1$, which result in modifications in expressions (2) and (3) being written as

$$P_k = \frac{|V_k||E|\sin(\delta_k)}{X} = \frac{|V_k||E|\delta_k}{X} \; k = 1, 2 \quad (4)$$

$$Q_k = \frac{|V_k|^2 - |V_k||E|\cos(\delta_k)}{X} = \frac{|V_k|^2 - |V_k||E|}{X} \; k = 1, 2 \quad (5)$$

As a result, the active and reactive power flows are proportional to the angle and change in the amplitude of the voltage, respectively.

4. Proposed Control Technique

Figure 3 depicts the two-DGs-based adopted MG with the proposed control technique. The first DG consists of an 850V solar PV array (a PV array of 38 parallel strings of 24 series-connected modules), an input filtering capacitance (C_P), a BB converter, and an inverter. The second is identical, but it operates on an 850V battery source. C_P guarantees

that the PV panel or battery functions as a DC voltage source. In the BB converter, silicon carbide MOSFET conduction determines circuit operation. In the on-state: the inductor current increases, placing the diode in a block state. In the off-state: the diode commutates and conducts because the inductor current cannot abruptly change. The inductor current decreases as energy is transferred to the capacitor. There are two operational limits for this circuit. When the duty cycle (D) of a PWM signal is zero, the output voltage is also zero, and when it is one, the output voltage grows to negative infinity. For operation in a continuous conduction mode, the output voltage is defined as follows: output voltage = $-D/(1-D)$ input voltage. As a result, the BB converter is utilized to generate a stable DC output voltage that is either higher or lower than the DC input voltage using the SMC technique. SMC methodology has been widely adopted due to its favorable robustness properties, which allow it to successfully model parameter uncertainties and external disturbances while still easily mathematically calculating the control parameters. For the first BB-based DG, it precisely produces a DC voltage of 250 volts, and for the second, it generates 400 volts. For testing the two SMC-based adopted BB converters, the input is set to different voltage values for buck (850V input exceeds output), boost (output exceeds input), and one as buck and one as boost. Following the stabilization of the DC bus by the SMC-based BB converters to supply the inverter with a constant desired DC voltage, discrete-time PQ control is proposed to control the load power sharing of the parallel inverters and achieve a stable AC bus. The PQ control method utilized a PR controller for rapid reference signal tracking, sensitivity to grid frequency drift, and absence of steady-state error. The utility grid and adopted DGs power the load, making the MG self-sufficient. If the DGs' power is less than load power, the grid injects the shortage. If the DGs generate more power than needed, the surplus will be returned to the grid. Detailed information about the proposed system's power circuit and control parameters are presented in Tables 1–4.

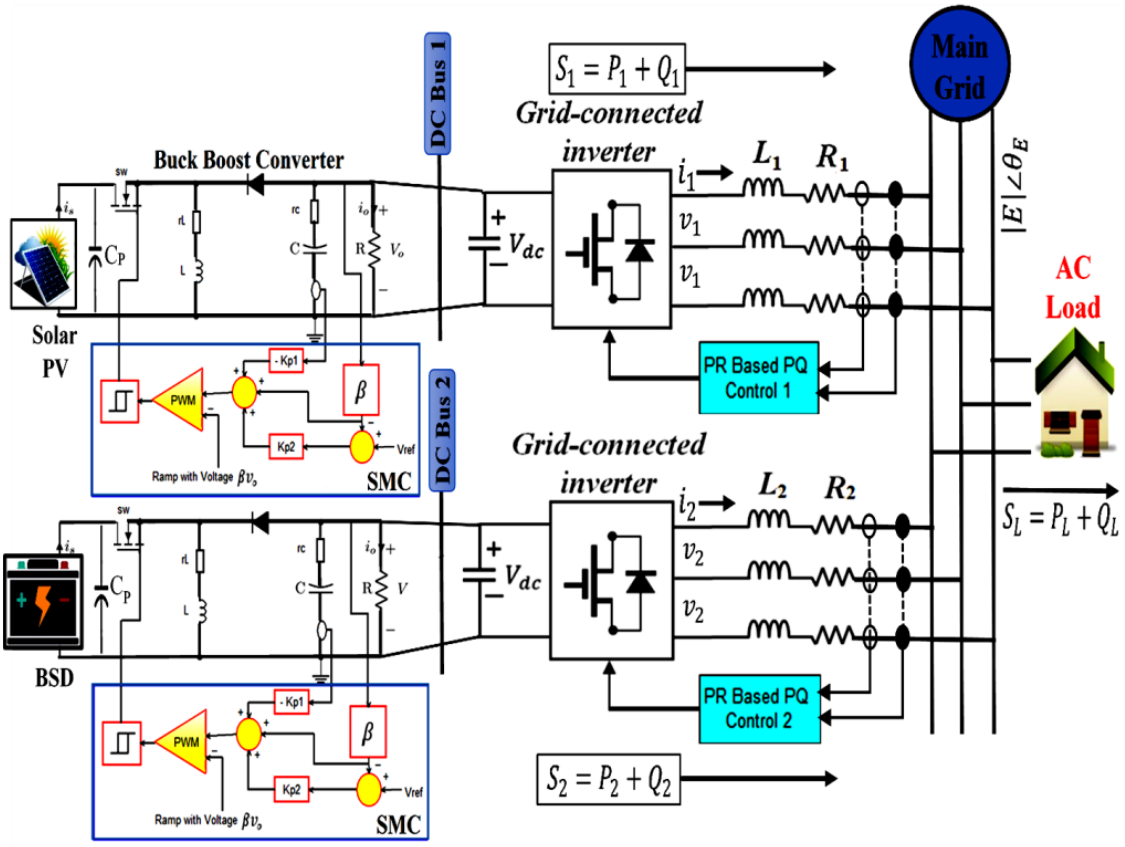

Figure 3. The two-DGs-based adopted MG system.

Table 1. The adopted SMC parameters.

Description	Symbol	Nominal Value
Settling time of SMC	T_S	1.5 msec
SM damping coefficient	ξ	1.34
Ratios of the SM coefficients	$\propto_1$ / $\propto_2$ and $\propto_3$ / $\propto_2$	19,939 and 102,846,495
Beta of SM	β	850/250 and 850/400
SM control gains	K_{P1} and K_{P2}	1 and 4.53

Table 2. The control parameters of the inverters.

Parameter Name	Acronym	Value
Bandwidth revolves around AC frequency ω_o	ω_c	$2 * pi * 3$
AC nominal frequency	$\omega_r = \omega_o$	$2 * pi * 50$
Proportional gain PR voltage compensator	k_{Pp}	22
Integral gain PR voltage compensator	k_{Rp}	22
Damping coefficient PR current and power compensators	ζ	0.95
Proportional gain PR current compensator	k_{Pi}	0.027
Integral gain PR current compensator	k_{Ri}	4.38
Measured signal gain for DG1 and DG 2	H_i	1

Table 3. Power and current loops' PR resonant filter parameters.

Parameter Name	Acronym
b_0	$1.146039290275440 \times 10^4$
b_1	0
b_2	$-1.146039290275440 \times 10^4$
a_0	1
a_1	−1.999976025486589
a_2	0.999976124181453

4.1. SMC for BB-Converter-Based DC MG Control

The SMC process is depicted in Figure 4 as having two phases. The first phase is the reaching phase, whereby the controlled system's feedback trajectory S is forced to move towards the sliding manifold via sliding control (Figure 4(1a)). This phase is completed when the hitting condition is satisfied. To satisfy the hitting condition, a sequence of control decisions is made to direct the controlled system's feedback trajectory away from sliding manifold = 0 (regardless of its current location, in other words, regardless of its initial conditions) toward the sliding manifold within proximity, as illustrated in Figure 4(2).

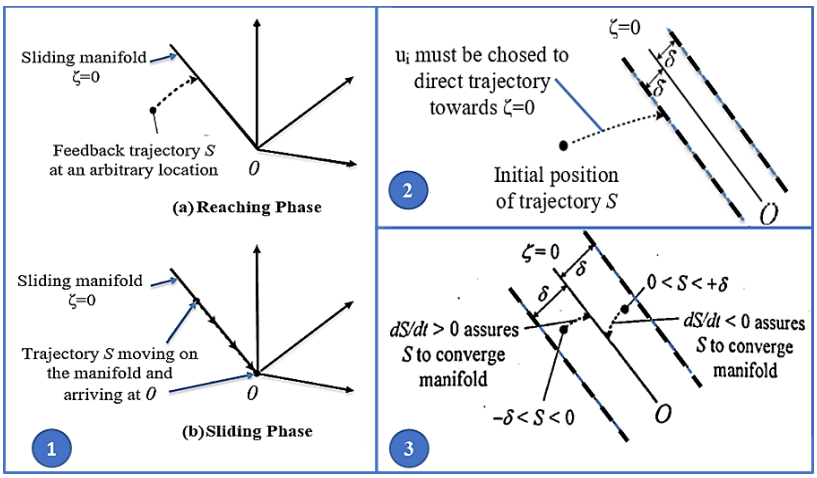

Figure 4. The SMC process works (**1**): (**a**) reaching phase, (**b**) sliding phase; trajectory movement according to hitting (**2**) and existence (**3**) conditions.

In the second phase, named the sliding phase, S moves on to the sliding plane (S = 0). That is what happens in Phase 2. It makes sure that S stays on the sliding manifold and moves toward the point of equilibrium, where it will eventually settle at "0". This means that the existence condition has been satisfied (to satisfy the existence condition, S must be designed in a way that it fulfills the condition of hitting, which has already been met within the neighboring regions ζ= 0 ($0 < |S| < \delta$) of the sliding manifold). Figure 4(3) shows how the trajectory is guaranteed to come back to the sliding manifold [35–37].

4.1.1. Control Gain Parameters of SMC

The schematic diagram in Figure 5 depicts a PID-based sliding mode voltage-controlled BB converter [30], where L, C, and R_L are the inductance, capacitance, and instantaneous load resistance of the DC/DC converter. The instantaneous currents of the inductance, capacitance, and load are denoted by i_L, i_C, and i_r, respectively. The instantaneous input voltage is denoted by v_i, the reference voltage is represented by V_{ref}, and the sensed output voltage is denoted by βv_o, where $\beta = \frac{R_2}{R_2+R_1}$, and the switching state of the converter's main switch is denoted by $u = 1$ or $u = 0$. The state control variables are $x_1 = -\left(\beta v_o - V_{ref}\right)$ (the voltage error), $x_2 = \dot{x_1} = \frac{d}{dt}\left(V_{ref} - \beta v_o\right) = -\beta\frac{dv_o}{dt} = -\beta\frac{dv_C}{dt} = -\beta\frac{i_C}{C}$ (changing the voltage error equation as time passes), and $x_3 = \int x_1 dt = -\int\left(\beta v_o - V_{ref}\right) dt$ (integral of the voltage error equation) [35].

(a) When MOSFET (switch S_W) *is ON*, u = 1 and then

$$-i_C = i_r = \frac{v_o}{R_L} \tag{6}$$

(b) When switch S_W *is OFF*, u = 0 and then

$$-i_C = -i_L + i_r = \int \frac{v_o}{L} dt - \frac{1}{R_L} v_o \tag{7}$$

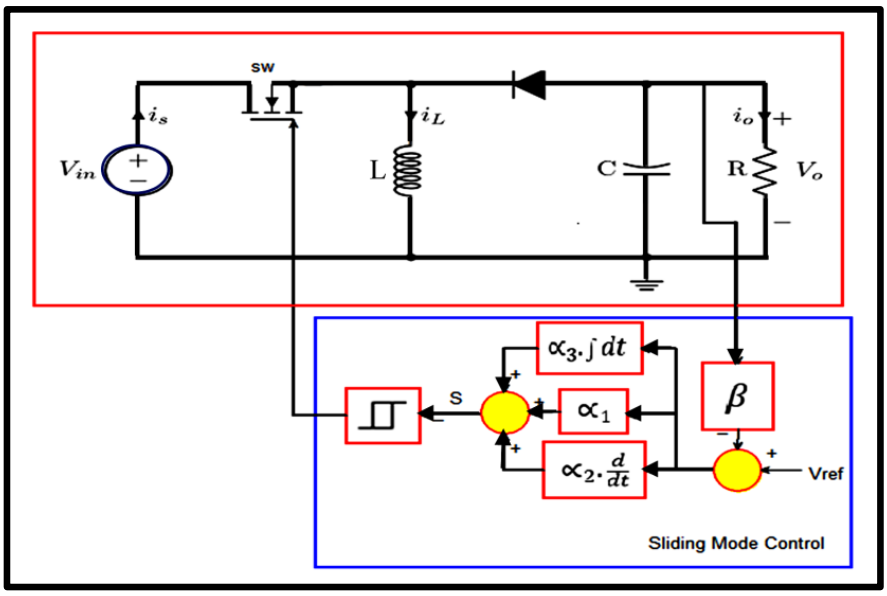

Figure 5. A schematic diagram of a PID-based sliding mode voltage-controlled BB converter.

Consequently, during the total commutation period T,

$$-i_C = \frac{1}{R_L} v_o + \int \frac{v_o\,\overline{u}}{L} dt\ ,\ \overline{u} = 1 - u \tag{8}$$

by substituting Equation (8) in x_2, obtaining new x_2; thus, the state new variables are in vector x, where $x = \begin{bmatrix} x_1 & x_2 & x_3 \end{bmatrix}^T$. By differentiating x with respect to time, it is possible to obtain the state-space description of the BB converter for the purpose of designing the controller.

$$\dot{x} = \begin{bmatrix} \dot{x_1} \\ \dot{x_2} \\ \dot{x_3} \end{bmatrix} = \begin{bmatrix} x_2 \\ -\frac{1}{R_L C} x_2 + \frac{\beta \overline{u} v_o}{LC} \\ x_1 \end{bmatrix} = \begin{bmatrix} 0 & 1 & 0 \\ 0 & -\frac{1}{R_L C} & 0 \\ 1 & 0 & 0 \end{bmatrix} \begin{bmatrix} x_1 \\ x_2 \\ x_3 \end{bmatrix} + \begin{bmatrix} 0 \\ \frac{\beta}{LC} v_o \\ 0 \end{bmatrix} \overline{u} = Ax + Bv + D \quad (9)$$

where $D = [000]^T$.

Consider the SMC law when designing the BB converter's fixed-frequency PWM SM controller

$$u = \begin{cases} 0 \text{ when } S < 0 \\ 1 \text{ when } S > 0 \end{cases} \quad (10)$$

where S stands for the feedback state variable's trajectory,

$$S = \sum_{i=1}^{k} \alpha_i x_i(t) \quad (11)$$

where $x_i(t) \in X(t)$ and $\alpha_i \; for \; i = 1 \overset{to}{\rightarrow} k$ are control parameters, also known as sliding coefficients, and thus [35,38],

$$S = \propto_1 x_1 + \propto_2 x_2 + \propto_3 x_3 = J^T x \quad (12)$$

where $\propto_1$, $\propto_2$, and $\propto_3$ are the matrix's embedded sliding coefficients $J^T = \begin{bmatrix} \propto_1 & \propto_2 & \propto_3 \end{bmatrix}$.

As previously stated, the existence condition of the SMC sliding phase is satisfied when the next condition is satisfied, i.e.,

$$\lim_{S \to 0} S \cdot \dot{S} < 0 \quad (13)$$

Hence, to satisfy Equation (13), when $S \rightarrow 0^+$ then $\dot{S}$ is negative ($v_{S \to 0^+}$ in Equation (13)), but $\dot{S}$ is positive for $S \rightarrow 0^-$. From Equation (9), when $S \rightarrow 0^+$, $v_{S \to 0^+} = \overline{u} = 0$, and when $S \rightarrow 0^-$, $v_{S \to 0^-} = \overline{u} = 1$, as well as by substituting $J^T = \begin{bmatrix} \propto_1 & \propto_2 & \propto_3 \end{bmatrix}$, which gives,

$$0 < \beta L \left(\frac{\propto_1}{\propto_2} - \frac{1}{R_L C} \right) i_C - LC \frac{\propto_3}{\propto_2} \left(V_{ref} - \beta v_o \right) < \beta v_o \quad (14)$$

The invariance conditions are utilized in order to generate ueq, which is an equivalent control signal for the fixed-frequency PWM-based SM controller of the BB converters, $\dot{S} = 0$:

$$\dot{S} = J^T B \overline{u}_{eq} + J^T A x = 0 \quad (15)$$

$$\overline{u}_{eq} = -\left[J^T B \right]^{-1} J^T A x = -\frac{\propto_3 LC}{\propto_2 \beta} \left(\frac{V_{ref}}{v_o} - \beta \right) + \frac{\beta L}{\beta v_o} \left(\frac{\propto_1}{\propto_2} - \frac{1}{R_L C} \right) i_C \quad (16)$$

Because of that, $u_{eq} = 1 - \overline{u}_{eq}$, $0 < \overline{u}_{eq} < 1$, and multiplying the result of the inequality by βv_o yields,

$$0 < u_{eq}^* = LC \frac{\propto_3}{\propto_2} \left(V_{ref} - \beta v_o \right) - \beta L \left(\frac{\propto_1}{\propto_2} - \frac{1}{R_L C} \right) i_C + \beta v_o < \beta v_o \quad (17)$$

The inequality relationship $0 < v_c < \hat{v}_{ramp}$ can be found from the relation $0 < u_{eq} = d = \frac{v_c}{\hat{v}_{ramp}} < 1$. The control signal v_c and ramp voltage $\hat{v}_{ramp}$ (variable in mag-

nitude) for the fixed-frequency PWM-based SM controller can then be obtained by comparison to Equation (17), such that [35]

$$\begin{aligned} u_{eq}^{*} &= LC\frac{\propto_3}{\propto_2}\left(V_{ref}-\beta v_o\right)-\beta L\left(\frac{\propto_1}{\propto_2}-\frac{1}{R_L C}\right)i_C+\beta v_o \\ &= -K_{P1}i_C+K_{P2}\left(V_{ref}-\beta v_o\right)+\beta v_o \end{aligned} \tag{18}$$

where K_{P1} is the constant gain of the signal from the capacitor current feedback, K_{P2} is the constant gain of the signal from the voltage error feedback, and $\hat{v}_{ramp} = \beta v_o$, as shown in Figure 3.

4.1.2. Sliding Coefficient Ratios

The magnitude of the output voltage of the BB may be less or greater than the magnitude of the input voltage and have the opposite polarity, depending on the arrangement of the components used to implement the BB circuit. The output voltage can be varied linearly between 0 and (+/−)V by adjusting the MOSFET's duty cycle [39,40]. Figure 3 depicts the graphical diagram of the fixed-frequency PWM-based SMC buck–boost converter.

It is understood that the controller's robustness over time to variations in line and load is the result of the nonlinear nature of the SMC, which has been built by additional βv_o components for BB converters, where βv_o is the instantaneous output voltage.

The sliding coefficient ratios ($\propto_1$ / $\propto_2$ and $\propto_3$ / $\propto_2$) must be calculated in order to compute the constant control gains K_{P1} and K_{P2} of the SMC. The damping coefficient (ξ) value and the desired settling time (Ts) can be used to calculate the sliding coefficients, which describe the different types of system responses: under-damped response when $0 \leq \xi < 1$; critically damped response when $\xi = 1$; and over-damped response when $\xi > 1$ [41].

Equation (12) will be rearranged and time differentiated to give,

$$\frac{\propto_3}{\propto_2}x_1+\frac{\propto_1}{\propto_2}\frac{dx_1}{dt}+\frac{d^2x_1}{dt^2} = {w_n}^2x_1+2\xi w_n\frac{dx_1}{dt}+\frac{d^2x_1}{dt^2} = 0 \tag{19}$$

where $w_n = \sqrt{\frac{\propto_3}{\propto_2}}$ is the undamped natural frequency, and $\xi = \frac{0.5\propto_1}{\sqrt{\propto_2 \propto_3}}$ and $\frac{\propto_3}{\propto_2} = \frac{0.25}{\xi^2}\left(\frac{\propto_1}{\propto_2}\right)^2$ [42].

Table 4. The adopted parameters of a DC/DC BB converter.

Description	Symbol	Nominal Value	Unit
Input voltage	V_i	850	V
Output voltages	V_o	250 (DG1) and 400 (DG2)	V
Main capacitor	C	1000	µF
Main capacitor-resistance	rc	36	mΩ
Main inductor	L	200	µH
Main inductor-resistance	rL	0.12	Ω
Switching frequency [43,44]	F_s	200	kHz
Load resistance	R_L	140	Ω
Input capacitor	C_p	500	µF

ξw_n denotes the rate of decay in the system response with an under-damped response; therefore, the time constant is,

$$\tau = \frac{1}{\xi w_n} = 2\frac{\propto_2}{\propto_1} \tag{20}$$

Assume Ts = 5 s for all ξ values ($0 \leq \xi < 1$, $\xi = 1$, and $\xi > 1$), which indicates that the system requires 5 s to reach steady-state operation and, thus,

$$\frac{\propto_1}{\propto_2} = \frac{1}{0.1T_S} \; and \; \frac{\propto_3}{\propto_2} = \frac{1}{0.04\xi^2 T_S^2} \tag{21}$$

However, in the case of critical-damped response systems,

$$\tau = \frac{1}{w_n} = \sqrt{\frac{\alpha_2}{\alpha_3}} \tag{22}$$

Using Equation (21) with $\xi = 1$ yields,

$$\tau = \frac{\propto_2}{0.5 \propto_1} \tag{23}$$

$$\frac{\propto_1}{\propto_2} = \frac{1}{0.1T_S} \text{ and } \frac{\propto_3}{\propto_2} = \frac{1}{0.04T_S^2} \tag{24}$$

and for over-damped response systems [35],

$$\tau = \frac{1}{-\left(\sqrt{\xi^2 - 1} - \xi\right) w_n} = \frac{2}{1 - \sqrt{1 - \frac{1}{\xi^2}}} \frac{\propto_2}{\propto_1} \tag{25}$$

From Equations (21) and (25),

$$\frac{\propto_1}{\propto_2} = \frac{1}{0.1\left(1 - \sqrt{1 - \frac{1}{\xi^2}}\right) T_S} \text{ and } \frac{\propto_3}{\propto_2} = \frac{1}{0.04\left(\xi - \sqrt{\xi^2 - 1}\right) T_S^2} \tag{26}$$

As a result, the sliding coefficient ratios ($\propto_1$ / $\propto_2$ and $\propto_3$ / $\propto_2$) can be calculated by first determining the required settling time and damping coefficient value, which implicitly specifies the response type. Table 4 shows the adopted DC/DC BB converter's power circuit parameters, while Table 1 shows the SMC parameters.

4.2. Decentralized PQ Control Based on Digital PR Controllers

The PQ control method of each inverter employs double control loops, as shown in Figure 6. The outer power loop generates the reference current in accordance with the power reference, whereas the current inner loop acts as a fine-tuning circuit. Due to the fact that the synchronous frame controller eliminates steady-state error and provides a rapid transient response, current control is accomplished in the synchronous dq reference frame.

Suppose that the reference active power is positive. The DG currents will flow between the inverters and the grid, indicating phase alignment with the voltage at the PCC. The grid current is a 180° phase with voltage and is equal to the sum of DG inverter currents. Altering the reactive power's reference value results in corresponding changes. Once the active power reference becomes negative, the newly generated energy is consumed by the power grid and converted into electricity. A 180° phase difference will be created between the two currents and voltages at the PCC point during the transfer of the current from the grid to the DG inverters during this process. A phase-locked grid current will be generated in response to a voltage change, with a magnitude equal to the sum of the inverter currents generated by the DGs. There will be no reactive power in this case, and the amount of reactive power can be adjusted by changing the reference point.

In Figure 6, once a periodic set of three-phase voltages and currents is applied, the active and reactive power calculation block computes the three-phase instantaneous active power P (in Watts) and reactive power Q (in VAR) [45]. The following formulae can be employed in order to carry out the calculations:

$$P = I_a \cdot V_a + I_b \cdot V_b + I_c \cdot V_c \tag{27}$$

$$Q = \frac{1}{\sqrt{3}}[(V_b - V_a) \cdot I_a + (V_c - V_a) \cdot I_b + (V_a - V_b) \cdot I_c] \tag{28}$$

where V_a, V_b, and V_c are the PCC voltages; I_a, I_b, and I_c are the inverter output currents.

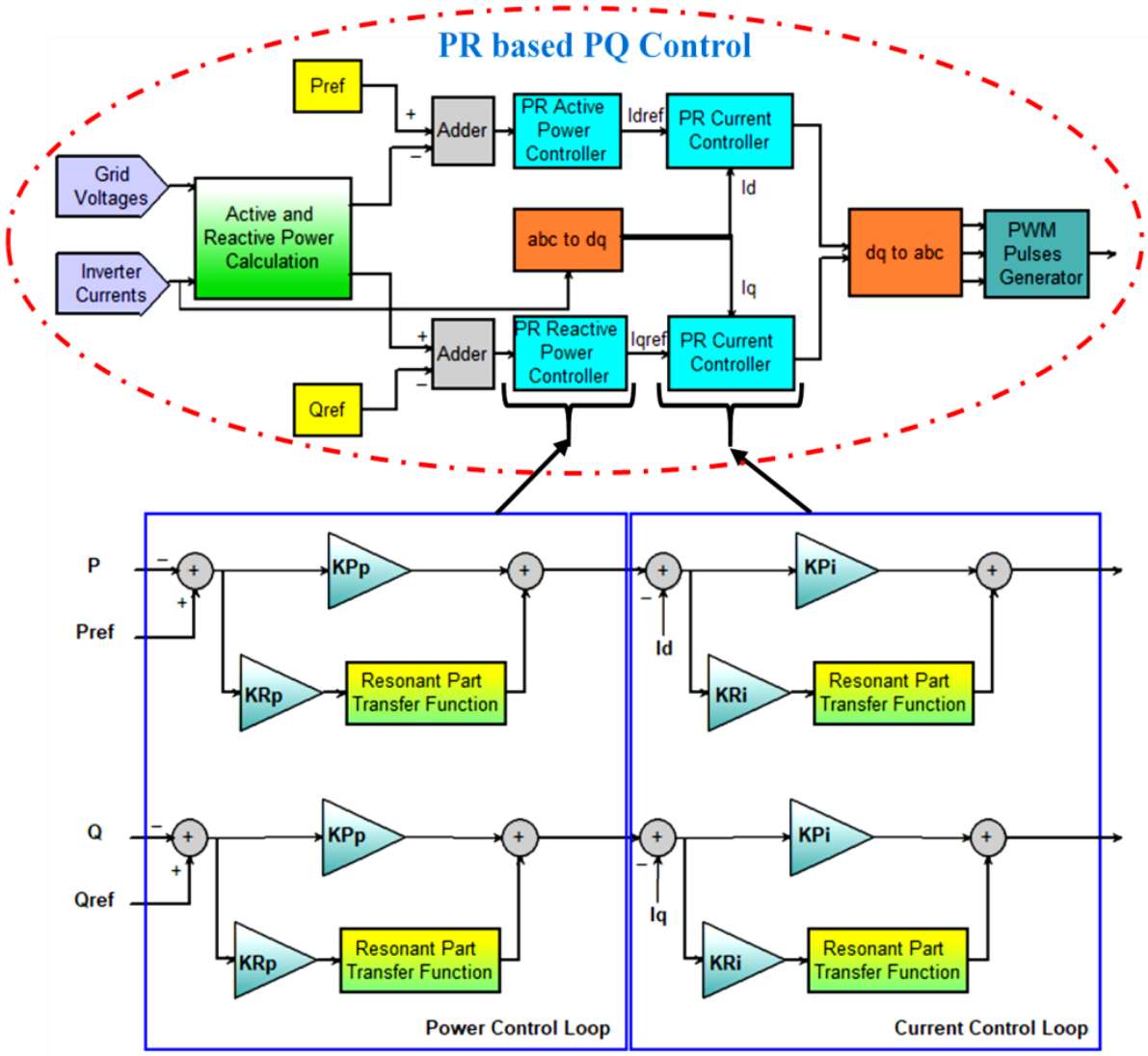

Figure 6. The proposed control technique of one inverter.

Then, the outer power loop creates the reference currents in accordance with the power target using two digital PR controllers for active and reactive power. The inner current loop compares the reference currents in the synchronous reference frame against their measured values to generate two error signals (for the d- and q-axes) that are applied to the two PR controllers in order to generate the reference voltage. The transfer function of the ideal PR controller is given as follows [46]:

$$G_{PRv}(s) = k_P + k_R \frac{s}{s^2 + \omega_o^2} \tag{29}$$

where k_P represents the controller's proportional gain, k_R represents the controller's resonant gain, and ω_o represents the resonant frequency, which is actually the grid frequency.

The ideal PR controller is difficult to implement because it acts like an infinite quality factor system. As a result, a non-ideal PR controller transfer function is as follows [46]:

$$G_{PRv}(s) = k_P + k_R \frac{2\omega_c s}{s^2 + 2\zeta\omega_c s + \omega_o^2} \tag{30}$$

where ω_c denotes the bandwidth centers around ac frequency ω_o and ζ denotes the damping factor.

Analog controller discretization can be investigated using Tustin's method [47]. This relationship replaces each *S*-domain in analog controllers with a *Z*-domain, according to the relationship (31).

$$s = \frac{z-1}{\frac{T}{2}(z+1)} \tag{31}$$

where T is the sampling period.

$$\begin{aligned} G_{PRv}\left(\frac{z-1}{\frac{T}{2}(z+1)}\right) &= k_P + k_R \frac{2\omega_c\left(\frac{z-1}{\frac{T}{2}(z+1)}\right)}{\left(\frac{z-1}{\frac{T}{2}(z+1)}\right)^2 + 2\zeta\omega_c\left(\frac{z-1}{\frac{T}{2}(z+1)}\right) + \omega_o^2} \\ &= k_P + k_R G_R(z) \end{aligned} \tag{32}$$

The *Z*-domain defines the resonant path, which is coherent with the gain k_R and the resonant IIR filter function $G_P(z)$ given in Equation (33) [48,49].

$$G_P(z) = \frac{b_0 + b_1 z^{-1} + b_2 z^{-2}}{a_0 + a_1 z^{-1} + a_2 z^{-2}} \tag{33}$$

where $b_0,\ b_1, b_2$ denote the feedback route parameters of the filter and $a_0,\ a_1, a_2$ denote the feedforward route parameters. In Equation (33), the value of a_0 is deliberately set to 1 so that the difference equation can be written as follows:

$$y(n) = -a_1 y(n-1) - a_2 y(n-2) + b_0 u(n) + b_1 u(n-1) + b_2 u(n-2) \tag{34}$$

where $y(n)$ represents the resonance filter output and $u(n)$ represents the resonance filter input.

This is one of the most significant contributions of this work. Using the resonant frequency, the controller can determine the frequency at which it should act in order to attain zero steady-state error. When only the preferred filter frequency response in the S-domain is known, the designer can use this information to compute the resonant filter coefficients using Tustin's method or by using Equations (35)–(43) [48,50].

$$k_p = \frac{\left(\sqrt{2\zeta+1}\right)(2\zeta+1)\omega_r L_o - R_0}{V_{dc}} \frac{1}{H_i} \tag{35}$$

$$k_R = \frac{\left[(2\zeta+1)^2 - 1\right]\omega_r{}^2 L_o}{2V_{dc}} \frac{1}{H_i} \tag{36}$$

where H_i denotes the measured signal gain, R_0 and L_0 are the line resistor and inductor of the inverter, and V_{dc} is the DC input voltage of the inverter.

$$b_0 = k_r B_r T_a \tag{37}$$

$$b_1 = T_a\left[-k_r B_r e^{-0.5 B_r T_a}\cos\left(T_a\sqrt{\omega_r^2 - \frac{1}{4}B_r^2}\right) - C\right] \tag{38}$$

where C is a constant with the following definition:

$$C = \frac{0.5 k_r B_r^2}{\sqrt{\omega_r^2 - \frac{1}{4}B_r^2}} e^{-0.5 B_r T_a}\cos\left(T_a\sqrt{\omega_r^2 - \frac{1}{4}B_r^2}\right) \tag{39}$$

$$b_2 = 0 \tag{40}$$

$$a_0 = 1 \tag{41}$$

$$a_1 = -2e^{-0.5 B_r T_a}\cos\left(T_a\sqrt{\omega_r^2 - \frac{1}{4}B_r^2}\right) \tag{42}$$

$$a_2 = e^{-B_r T_a} \tag{43}$$

where ω_r denotes the angular frequency of the resonance, bandwidth B_r is the angular resonant frequency, T_a denotes the sampling time, and k_r denotes the resonance gain.

The outputs of the current control subsystem are the voltage signals in the synchronous reference frame (V_d and V_q), which have been used to generate the three-phase reference signal of the inverter output voltage. The dq0 to abc frame transformation is required to transfer the (dq) frame voltage signals into the related three phases (abc) using Equation (44); the inverse of this transformation is given in Equation (45) [51],

$$\begin{bmatrix} a \\ b \\ c \end{bmatrix} = \begin{bmatrix} \cos(\theta) & -\sin(\theta) & 1 \\ \cos(\theta - \frac{2\pi}{3}) & -\sin(\theta - \frac{2\pi}{3}) & 1 \\ \cos(\theta + \frac{2\pi}{3}) & -\sin(\theta + \frac{2\pi}{3}) & 1 \end{bmatrix} \begin{bmatrix} d \\ q \\ 0 \end{bmatrix} \tag{44}$$

$$\begin{bmatrix} d \\ q \\ 0 \end{bmatrix} = \begin{bmatrix} \cos(\theta) & \cos(\theta - \frac{2\pi}{3}) & \cos(\theta + \frac{2\pi}{3}) \\ -\sin(\theta) & -\sin(\theta - \frac{2\pi}{3}) & -\text{sine}(\theta + \frac{2\pi}{3}) \\ 0.5 & 0.5 & 0.5 \end{bmatrix} \begin{bmatrix} a \\ b \\ c \end{bmatrix} \tag{45}$$

Usually, the reference angle θ is measured by phase-locked loop (PLL) and written as $\theta = \omega t$, where ω is the frequency of the common AC bus, which must equal $(2\pi(50))$ when the grid frequency is 50 Hz.

The final block subsystem is the PWM pulse generator, which converts three-phase signals into pulses for the inverter's six power electronic switches. Table 2 shows the control parameters of the adopted inverters. The coefficients of the resonant filter part of both PR controllers for power and current loops are listed in Table 3.

The magnitude response of the adopted designed resonant filter in the frequency domain is shown in Figure 7a. The gain at 50 Hz only is 0 dB, demonstrating the resonant filter's effectiveness. In this case, just the component of the error at 50 Hz is multiplied by one. All other components' power is significantly reduced. Additionally, Figure 7a shows the phase response of the resonant filter in the frequency plane, which is shown at the bottom of Figure 7a. At the resonance, the phase shifts 180 degrees as a result of the poles of the transfer function being in phase. The magnitude response of the designed PR controller is illustrated in Figure 7b. The greatest amount of amplification occurs at a frequency of 50 Hz. The phase response of the designed PR controller is shown in the same figure. When low and high frequencies are used, they have up to a zero phase.

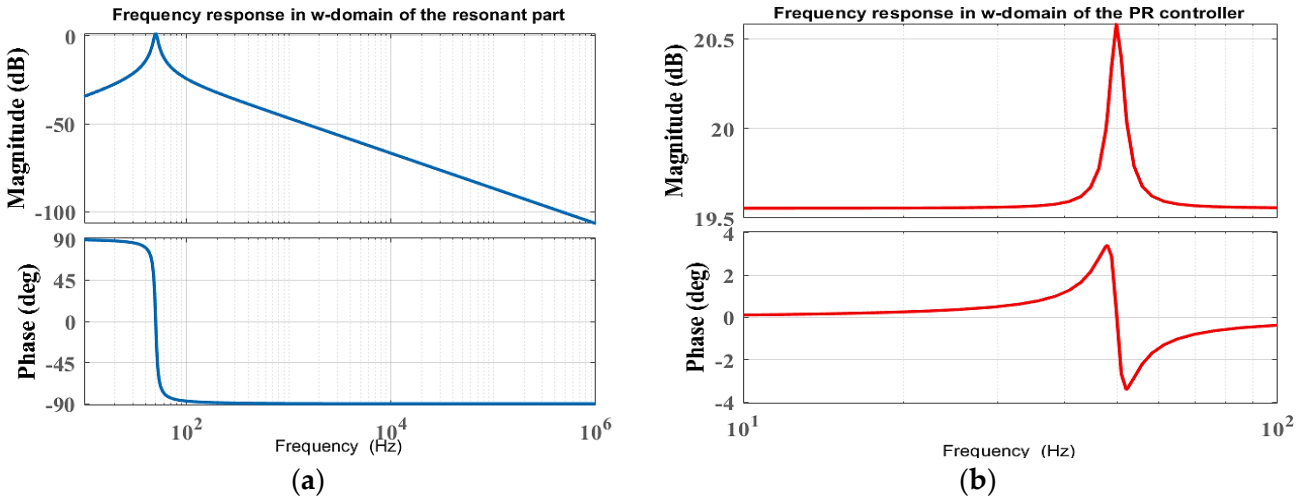

Figure 7. The magnitude and phase response of the designed (**a**) resonance filter and (**b**) PR controller.

5. Power Flow Control Based on MPC

Adaptable active and reactive power control is required to improve power quality and system stability. Hence, the FCS-MPC can be used for active and reactive power regulation.

The MPC selects the optimal voltage vector sequence for each inverter to meet load demand while maintaining power flow between the MG and the main grid. The FCS-MPC uses the discrete nature of power converters to speed up MPC calculations. Because each inverter has a limited number of switching states, the prediction procedure involves reducing the cost function.

5.1. System Modeling

Direct power control (DPC) is a strategy that uses a predictive model of instantaneous power evolution to control the power output. The following equations can be used to calculate the instantaneous active and reactive power of grid-connected inverters in the stationary reference frame (αβ) and for a three-phase symmetrical power system [30].

$$i_{k\alpha\beta}(i+1) = i_{i\alpha\beta}(k) + \frac{T_s}{L}\left[V_{i\alpha\beta}^{(lk)}(i) - V_{g\alpha\beta}(i) - Ri_{k\alpha\beta}(i)\right] \; k = 1,2 \text{ and } lk = 0,\ldots,7 \quad (46)$$

where l_k denotes the k-th inverter's possible switching state. The predicted grid current can be expressed as:

$$i_{o\alpha\beta}(i+1) = i_{k\alpha\beta}^{(l1)}(i+1) + i_{k\alpha\beta}^{(l1)}(i+1) - i_{L\alpha\beta}(i+1) \quad (47)$$

The available grid's active and reactive powers are defined as [30],

$$P(i) = 1.5\{V_{g\alpha}i_{o\alpha}(i) + V_{g\beta}i_{o\beta}(i)\} \quad (48)$$

$$Q(i) = 1.5\{-V_{g\beta}i_{o\alpha}(i) + V_{g\alpha}i_{o\beta}(i)\} \quad (49)$$

5.2. Cost Function

The power produced by the DGs is called P_{DG}, and the power demanded by the loads is called P_{Demand}. The net power supplied to the utility grid (P_{net}) can be calculated as follows:

$$P_{net} = P_{DG} - P_{Demand} \quad (50)$$

$$P_{DG} = P_1 + P_2 \quad (51)$$

where the P_1 and P_2 are the active power for the first and second DGs.

Thus, the predicted grid power can be obtained as the following [30]:

$$P_{net}(i+1) = 1.5\left\{V_{g\alpha}i_{o\alpha}(i+1) + V_{g\beta}i_{o\beta}(i+1)\right\} \quad (52)$$

$$Q_{net}(i+1) = 1.5\left\{-V_{g\beta}i_{o\alpha}(i+1) + V_{g\alpha}i_{o\beta}(i+1)\right\} \quad (53)$$

The grid voltage and current are measured at the current sampling time, and we apply Equations (46)–(53) to compute P_{net} and Q_{net} for all switching states of each inverter at the next sampling time. The cost function is defined as the following:

$$J = \left[P_{ref} - P_{net}(i+1)\right]^2 + \left[Q_{net} - Q_{ref}(i+1)\right]^2 \quad (54)$$

By minimizing the cost function, the optimal power flow between the two parallel DGs can be achieved, allowing for transmitted power to the utility grid at the scheduled reference levels (P_{ref} and Q_{ref}) and demanded power. Figure 8 shows the representation block diagram scheme and the flowchart of the MPC in (a) and (b), respectively.

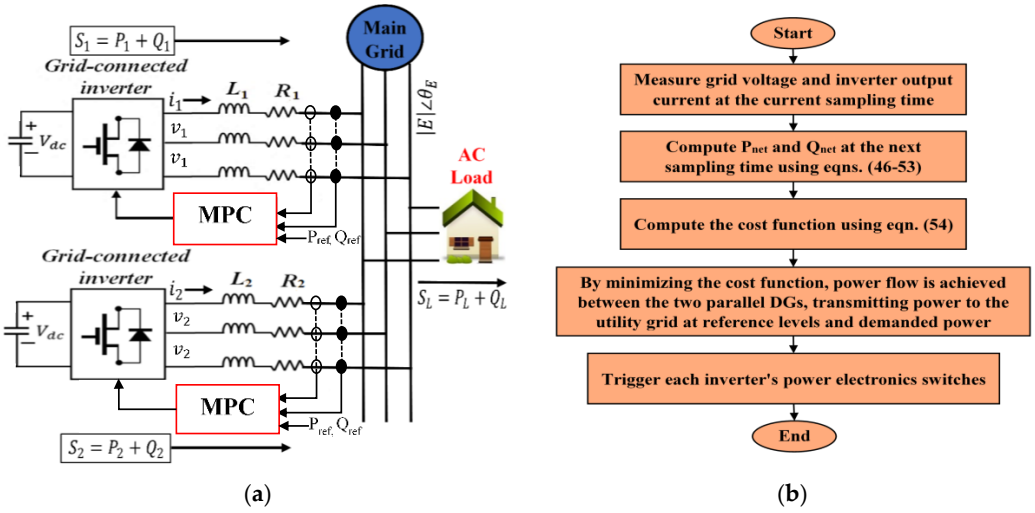

(**a**) (**b**)

Figure 8. (**a**) The representation block diagram scheme of MPC and (**b**) the MPC flowchart.

6. Simulation Results and Discussion

In this paper, the first case study includes two parallel three-phase DGs operating in a grid-tied mode, which is simulated in an MG application using MATLAB/Simulink, as shown in Figure 3. The MG parameters for this case study are listed in Table 5, which is based on reference [30].

Table 5. The MG parameters.

Description	Symbol	Nominal Value
Grid voltage	V_g	100 V
Active power of the load	P_L	3 kW
Power frequency	f	50 Hz
Sampling time	T_s	50 µs
DG1		
Line resistance	R_o	0.51 Ω
Line inductance	L_o	4.8 mH
DC input of BB converter	V_{dcs}	850 V
DC output of BB converter	V_{dco}	250 V
DG2		
Line resistance	R_o	1 Ω
Line inductance	L_o	10 mH
DC input of BB converter	V_{dcs}	850 V
DC output of BB converter	V_{dco}	400 V

The description of the used reference power signals to be tracked by each inverter is as follows: at the start, both the reference active and reference reactive power are set to zero. The active power is varied from 0 to −4 kW at 0.05 s, 0 W at 0.06 s, 3 kW at 0.07 s, and 0 W at 0.08 s and remains constant at 0 kW, whereas the reactive power reference is varied from 0 to −3 kVAR at 0.02 s, then returned to 0 at 0.04 s, becoming 1 kVAR at 0.09 s.

Figure 9 shows the output voltages of the BB converters of DG1 and DG2 utilizing the SMC as a control strategy. The figure shows that the DC bus voltages are steady at the reference points (250 V for DG1 and 400 V for DG2), and they are unaffected by rapid changes in load or input. For testing the two SMC-based BB converters, the input voltage is set to different values for the buck converter (input exceeds output; Figure 9a), boost converter (output exceeds input; Figure 9b), and one as a buck converter and one as a boost converter (Figure 9c). Since the input voltage is set to be greater than the first converter and less than the latter, the first converter behaves as a buck converter to reduce the voltage

to 250 V, and the second converter acts as a boost converter to increase the voltage to 400 V. In the presented case study, solar PVs and a storage device serve as inputs to the BB converters, which are used to generate 850 V for the adopted BB converters. Parallel DGs can make appropriate decisions in response to changes in power reference points. The controllers track the reference points in order to maintain the scheduled level of active and reactive power flows. Figure 10 shows the performance of the MPC technique for each individual DG [30], whereas Figure 11 illustrates the proposed technique's performance for each DG. Figure 12 shows the performance of power flow tracking in the case of parallel DGs. Because the load is only 3 kW, the reactive power to the grid is equal to the sum of the reactive power of both distribution generators (no reactive power load). In the time duration between 0.07 to 0.08 s, the total power from DGs is 6 kW, but only 3 kW is sent to the main grid because the load consumes 3 kW. Between 0.05 and 0.06 s, the total power from the main grid is equal to 11 kW, which is the sum of the DGs' total power (−8 kW) and the load power (3 kW). The PCC frequency is exactly 50 Hz, as shown in Figure 13. Figure 14 illustrates the PCC or common AC bus current and voltage in (a) and (b), respectively. The current and voltage can be seen, indicating that the performance of the system is stable. The proposed system performance is demonstrated by comparing the above AC bus voltage and power flow of each DG with the results of the MPC and droop control techniques presented in [30]. The results of the proposed discrete PR-based PQ technique are shown to be superior. It is proven that using the proposed method results in vastly improved power flow tracking.

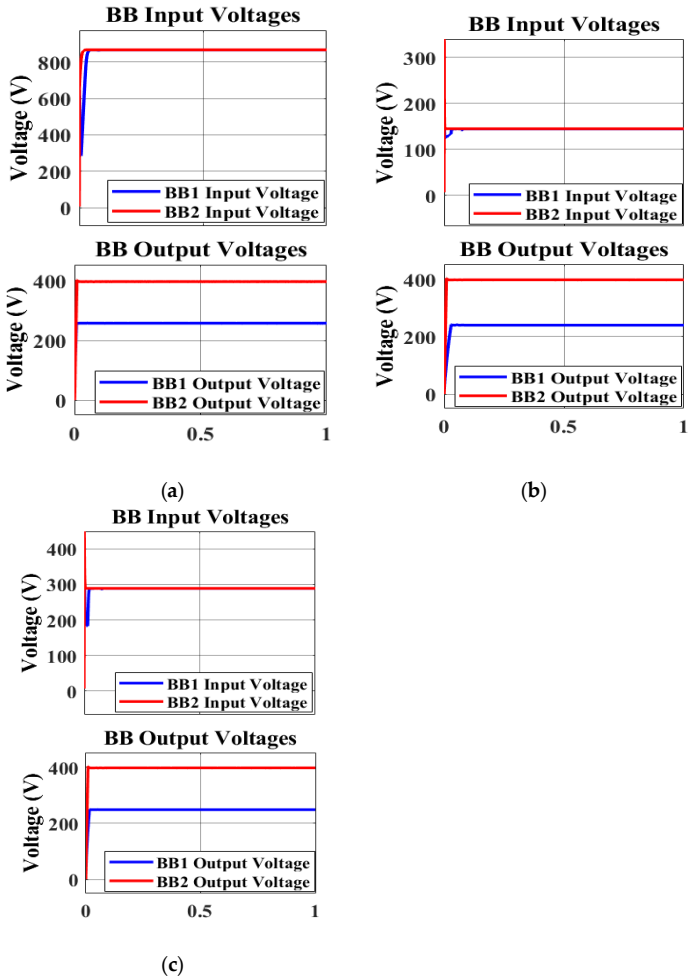

Figure 9. The input and output voltages of the BB converters' operation: (**a**) buck converters, (**b**) boost converters, and (**c**) the first converter is buck and the second is boost.

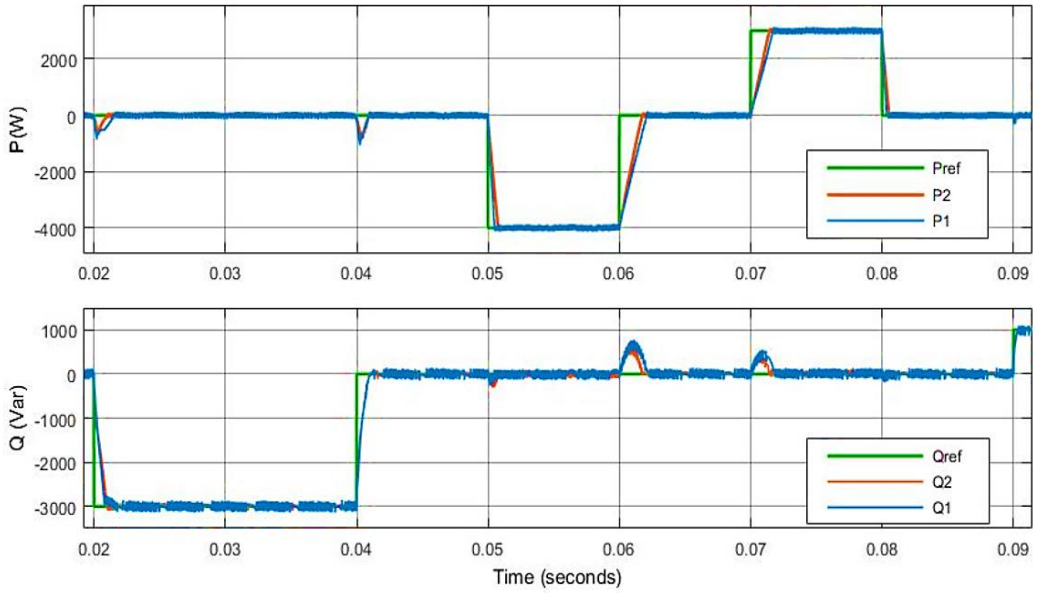

Figure 10. Individual DG power flow control using MPC.

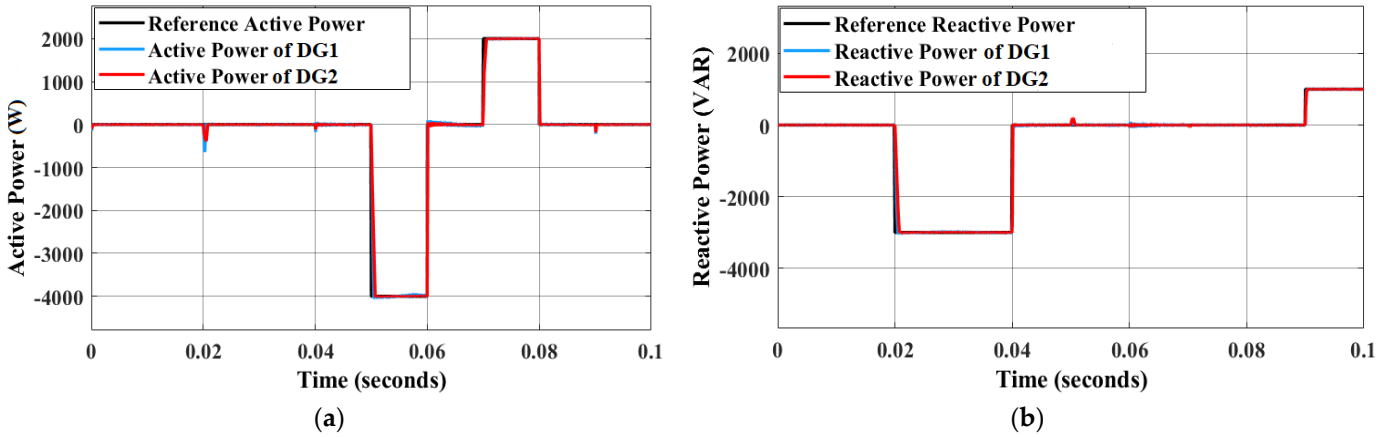

Figure 11. Individual DG power flow control using the proposed PQ control: (**a**) active power and (**b**) reactive power.

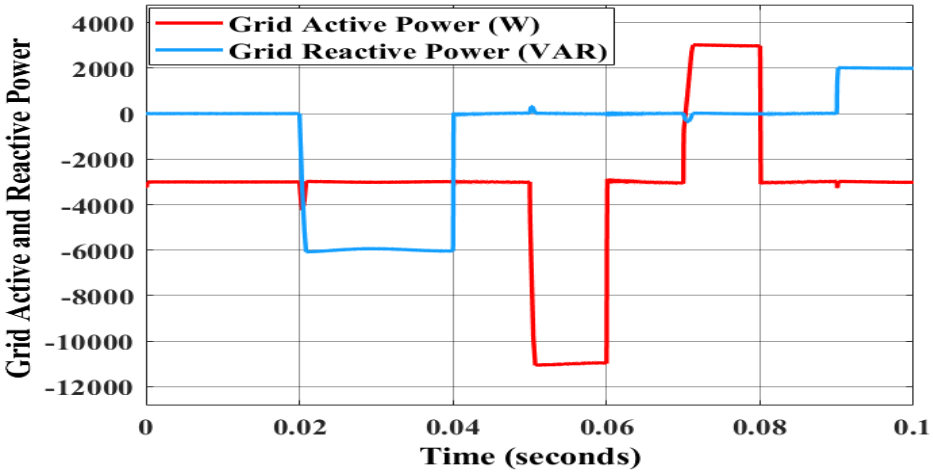

Figure 12. Active and reactive net power flows to the grid using PQ-control-based digital PR controllers.

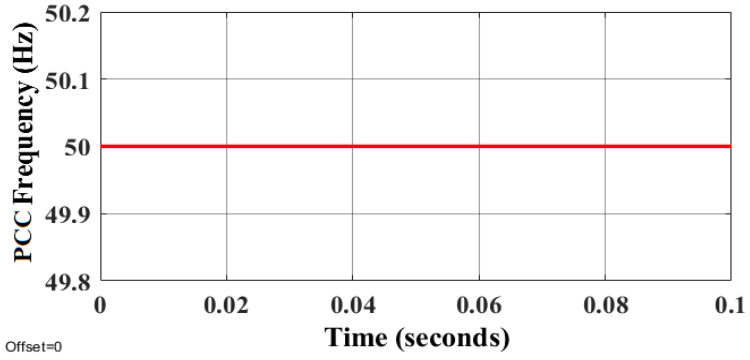

Figure 13. AC common bus frequency using the proposed technique.

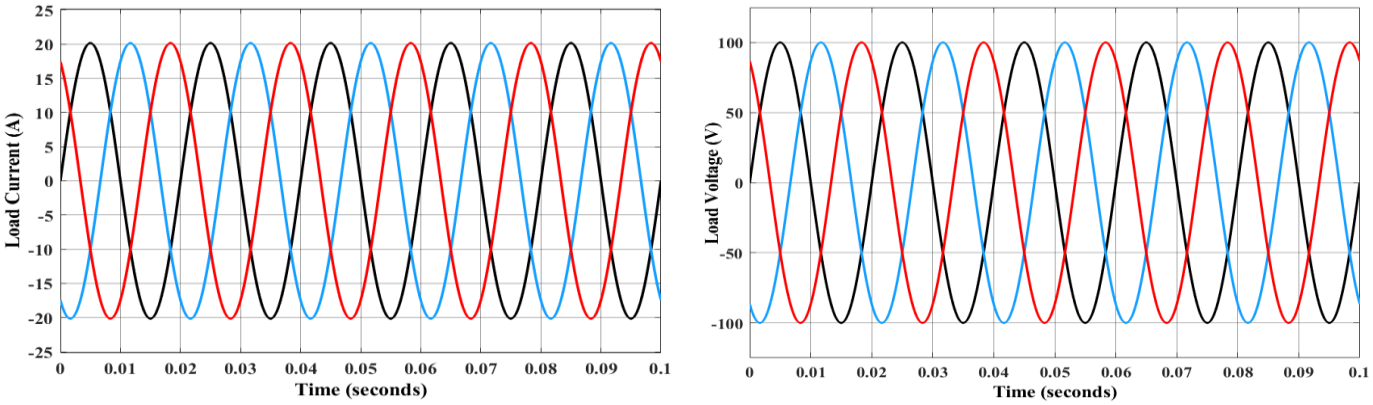

Figure 14. AC common bus current and voltage using the proposed technique: (**a**) current and (**b**) voltage signal.

Figures 15–17 show the active and reactive power of each DG, utility grid power, and PCC frequency, respectively, under changing load conditions, as follows: load at start = 3kW; then, it is increased to 6 kW (200%) at 0.4 s; then, it is increased to 300% at 0.8 s; then, it is decreased to 200% at 1.2 s; finally, it is returned to 100% at 1.6 s. The load current and voltage under this scenario are shown in Figure 18a,b, respectively. Clearly, each DG follows its reference power. Since the load is entirely active, the total reactive power on the grid is 8000 VAR, which is equal to the reference reactive power of two DGs added together. In spite of fluctuating loads, the voltage and frequency remain stable.

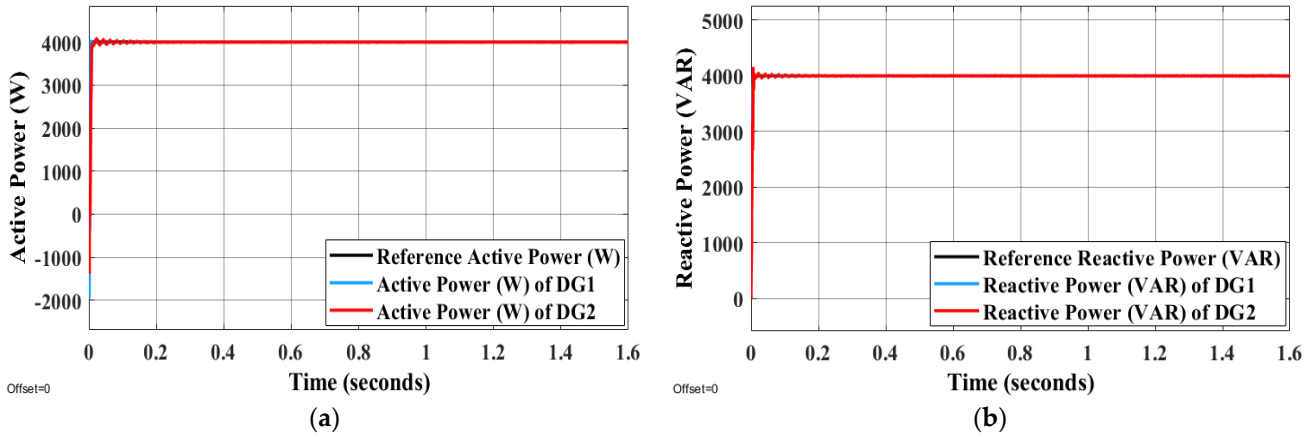

Figure 15. Individual DG power flow control using the proposed technique under changing load conditions: (**a**) active power and (**b**) reactive power.

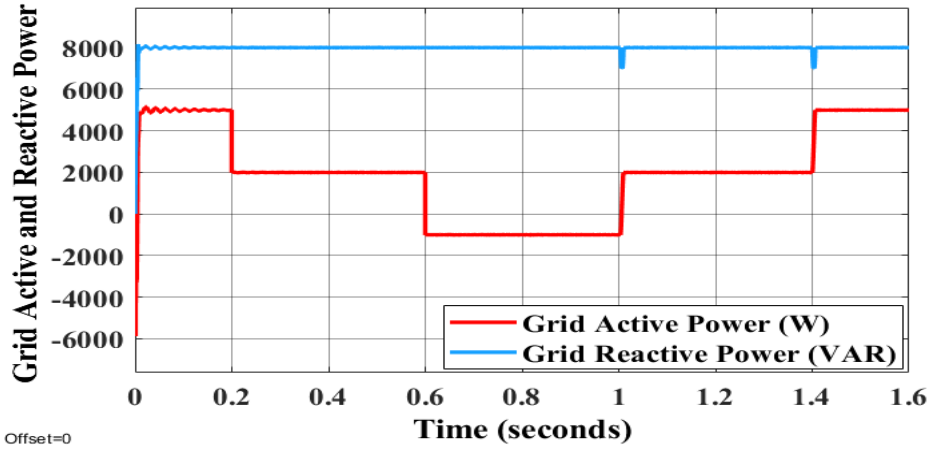

Figure 16. Active and reactive net power flows to the grid using the proposed technique under changing load conditions.

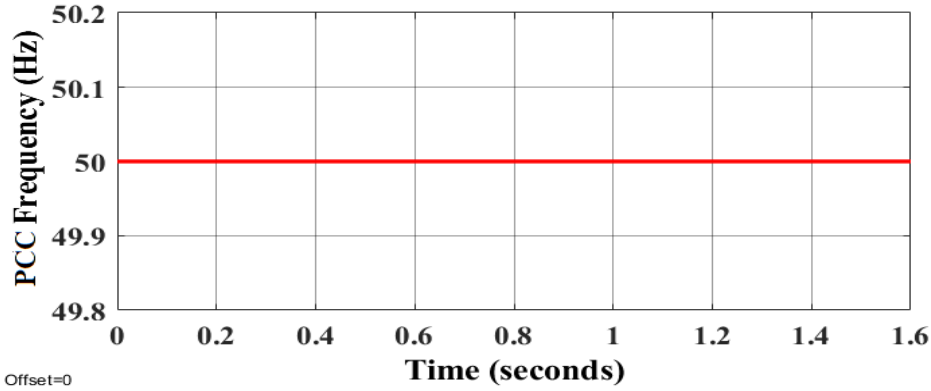

Figure 17. AC common bus frequency using the proposed technique under changing load conditions.

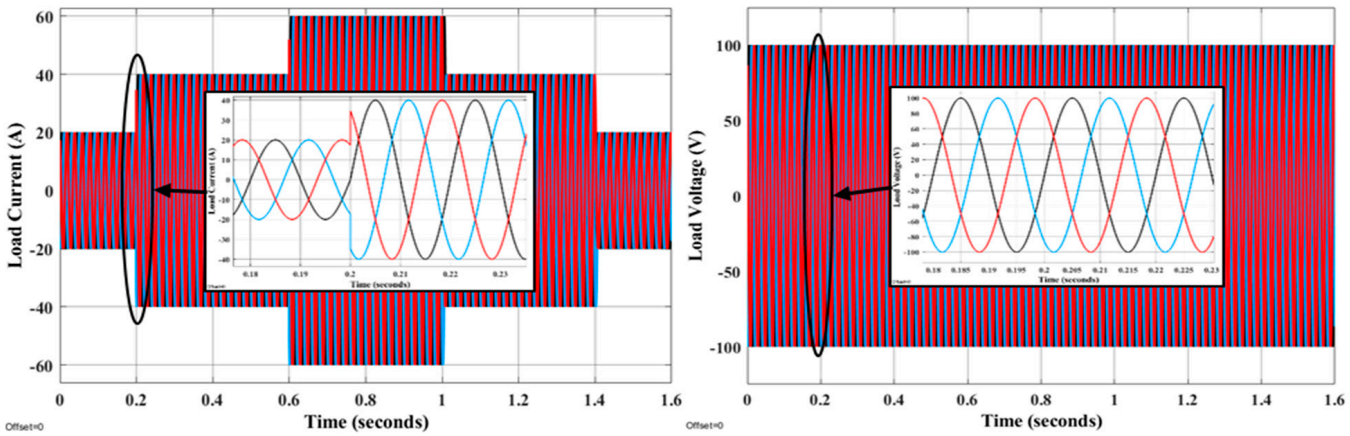

(**a**) (**b**)

Figure 18. AC common bus current and voltage using the proposed technique under changing load conditions: (**a**) current and (**b**) voltage signal.

The second case study extends the adopted MG into five parallel DGs. As depicted in Figure 19, the active and reactive power of each DG corresponds to its reference. As shown in Figure 20, if the third DG has outages within the time interval of [0.02 0.06] seconds, the other DGs can track the reference power signals correctly. Figure 21 illustrates the grid powers without or with the third DG failure.

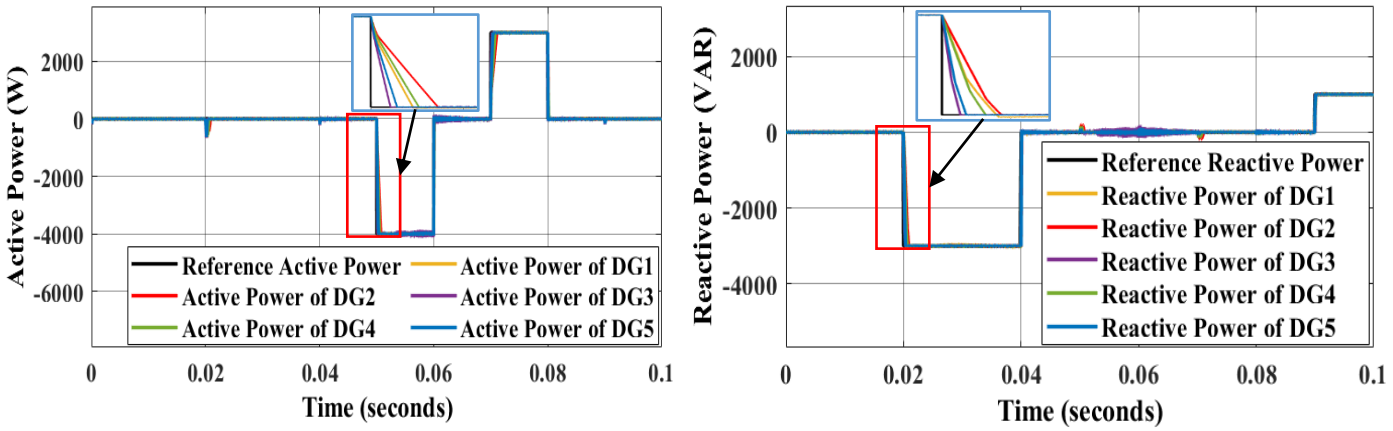

(**a**) (**b**)

Figure 19. Individual DG power flow control under the second case study without an outage DG: (**a**) active power and (**b**) reactive power.

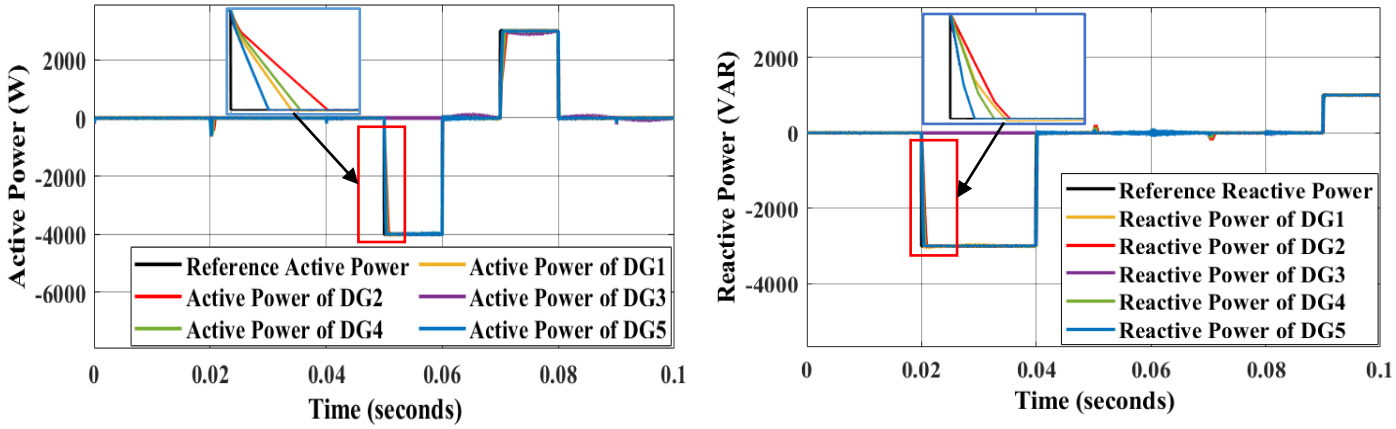

(**a**) (**b**)

Figure 20. Individual DG power flow control under the second case study with an outage third DG: (**a**) active power and (**b**) reactive power.

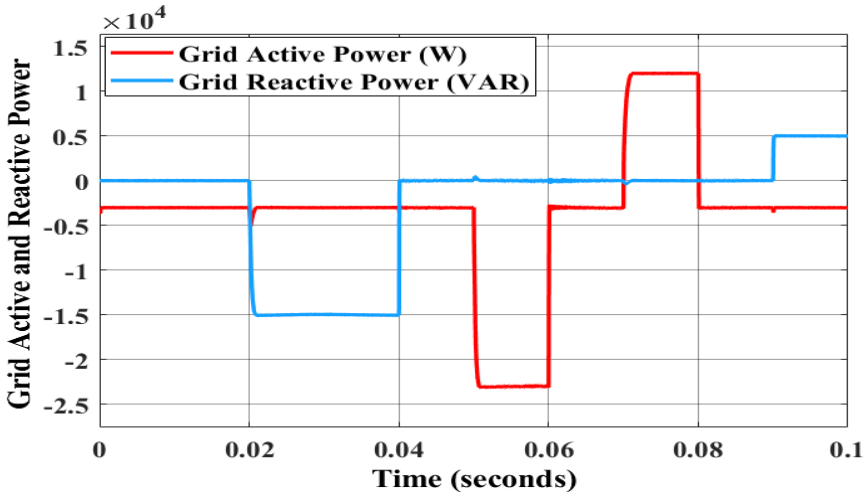

Figure 21. Active and reactive net power flows to the grid under the second case study without DG outage or with a third DG outage.

7. Conclusions

In this paper, a digital PQ-control-based PR controller is proposed to solve the power-sharing dilemma of parallel DGs in grid-tied MGs and to accomplish the stability objective. A PR controller is employed to get rid of harmonics by creating a high-gain digital IIR filter at the resonant frequency. The used PR controller can quickly track the reference signal, is sensitive to frequency changes on the grid, and produces no steady-state error. This paper discusses a power and current PR-controller-based inverter design. Step-by-step procedures are provided for calculating resonant and proportional gains and resonant path coefficients. A PR controller's frequency-domain analysis has also been discussed in this study. The PR controller's gain was 0 dB only at 50 Hz, proving the effectiveness of the resonant filter. In this case, only the frequency at 50 Hz is multiplied by one. Other components' power is greatly reduced. The resonance phase shifts 180 degrees because the transfer function poles are in phase. In addition, the nonlinear SMC control of the BB converter was utilized to avoid errors in inverter input voltage and provide each DG's inverter with the desired stable DC voltage (250 and 400 V for the first and second inverters, respectively). In high-signal operating conditions, SMC allows the controlled converters to operate flawlessly while maintaining efficient regulation and dynamic performance despite significant changes in the line, load, and parameters. The proposed PQ-based inverters operate following the stabilization of the DC buses. The proposed inverter control method is efficient and ensures that each inverter follows its reference active and reactive power. Furthermore, the DGs are capable of responding appropriately to changes in load and the failure of DGs, ensuring that the power flow to the main grid remains at the scheduled level at all times. By comparing with the results of the MPC and droop control techniques presented in [30], it can be said that the results of the proposed discrete PR-based PQ technique are superior to others in terms of improved system performance.

Author Contributions: Authors: A.M.J.: original draft, software, methodology, and validation; B.H.J.: supervisor, formal analysis, research resources, investigation, and editing and writing; B.H.J.: validation; B.-C.N.: visualization, project administration, and funding acquisition. All authors have read and agreed to the published version of the manuscript.

Funding: This research was supported by CEREM Department of the "Gheorghe Asachi" Technical University of Iasi, Romania.

Data Availability Statement: Not applicable.

Conflicts of Interest: The authors declare no conflict of interest.

References

1. Jasim, A.M.; Jasim, B.H.; Bureš, V. A novel grid-connected microgrid energy management system with optimal sizing using hybrid grey wolf and cuckoo search optimization algorithm. *Front. Energy Res.* **2022**, *10*, 960141. [CrossRef]
2. Jasim, A.M.; Jasim, B.H.; Kraiem, H.; Flah, A. A Multi-Objective Demand/Generation Scheduling Model-Based Microgrid Energy Management System. *Sustainability* **2022**, *14*, 10158. [CrossRef]
3. Alhasnawi, B.N.; Jasim, B.H.; Issa, W.; Anvari-Moghaddam, A.; Blaabjerg, F. A New Robust Control Strategy for Parallel Operated Inverters in Green Energy Applications. *Energies* **2020**, *13*, 3480. [CrossRef]
4. González, I.; Sánchez-Squella, A.; Langarica-Cordoba, D.; Yanine-Misleh, F.; Ramirez, V. A PI + Sliding-Mode Controller Based on the Discontinuous Conduction Mode for an Unidirectional Buck–Boost Converter with Electric Vehicle Applications. *Energies* **2021**, *14*, 6785. [CrossRef]
5. Sahoo, S.K.; Sinha, A.K.; Kishore, N.K. Control techniques in AC, DC, and hybrid AC–DC microgrid: A Review. *IEEE J. Emerg. Sel. Top. Power Electron.* **2018**, *6*, 738–759. [CrossRef]
6. Xin, H.; Zhang, L.; Wang, Z.; Gan, D.; Wong, K.P. Control of island AC microgrids Using a fully distributed approach. *IEEE Trans. Smart Grid* **2014**, *6*, 943–945. [CrossRef]
7. Jiang, Q.; Xue, M.; Geng, M. Energy management of microgrid in grid-connected and stand-alone modes. *IEEE Trans. Power Syst.* **2013**, *28*, 3380–3389. [CrossRef]
8. Colet-Subirachs, A.; Ruiz-Alvarez, A.; Gomis-Bellmunt, O.; Alvarez-Cuevas-Figuerola, F.; Sudria-Andreu, A. Centralized and distributed active and reactive power control of a utility connected microgrid using IEC61850. *IEEE Syst. J.* **2011**, *6*, 58–67. [CrossRef]
9. Jasim, A.M.; Jasim, B.H.; Mohseni, S.; Brent, A.C. Consensus-Based Dispatch Optimization of a Microgrid Considering Meta-Heuristic-Based Demand Response Scheduling and Network Packet Loss Characterization. *Energy AI* **2022**, *11*, 100212. [CrossRef]

10. Alhasnawi, B.; Jasim, B. Adaptive Energy Management System for Smart Hybrid Microgrids. The 3rd Scientific Conference of Electrical and Electronic Engineering Researches (SCEEER). *Iraqi J. Electr. Electron. Eng.* **2020**, 73–85. [CrossRef]
11. Arafat, M.N.; Elrayyah, A.; Sozer, Y. An Effective Smooth Transition Control Strategy Using Droop-Based Synchronization for Parallel Inverters. *IEEE Trans. Ind. Appl.* **2015**, *51*, 2443–2454. [CrossRef]
12. He, J.; Li, Y.; Harris, B. Investigation and active damping of multiple resonances in a parallel-inverter-based microgrid. *IEEE Trans. Power Electron.* **2013**, *28*, 234–246. [CrossRef]
13. Choi, W.; Lee, W.; Sarlioglu, B. Effect of grid inductance on grid current quality of parallel grid-connected inverter system with output LCL filter and closed-loop control. In Proceedings of the 2016 IEEE Applied Power Electronics Conference and Exposition (APEC), Long Beach, CA, USA, 20–24 March 2016.
14. Hu, J.; Zhu, J.; Guerrero, J.M. Model predictive control of smart microgrids. In Proceedings of the 2014 17th International Conference on Electrical Machines and Systems (ICEMS), Hangzhou, China, 22–25 October 2014; pp. 2815–2820.
15. Quevedo, D.; Geyer, T. Performance of multistep finite control set model predictive control for power electronics. *IEEE Trans. Power Electron.* **2015**, *30*, 1633–1644.
16. Aghdam, M.M.; Li, L.; Zhu, J.; Palizban, O. Finite Control Set Model Predictive Control-A Powerful Control Algorithm for Grid-Connected Power Converters. In Proceedings of the 2016 11th IEEE Conference on Industrial Electronics and Applications (ICIEA), Hefei, China, 5–7 June 2016.
17. Shuai, Z.; Sun, Y.; Shen, Z.J.; Tian, W.; Tu, C.; Li, Y.; Yin, X. Microgrid stability: Classification and a review. *Renew. Sustain. Energy Rev.* **2016**, *58*, 167–179. [CrossRef]
18. Jena, S.; Babu, C.; Mishra, G.; Naik, A. Reactive power compensation in inverter-interfaced distributed generation. In Proceedings of the 2011 International Conference on Energy, Automation, and Signal (ICEAS), Bhubaneswar, India, 28–30 December 2011; pp. 1–6.
19. Hornik, T.; Zhong, Q. A Current-control strategy for voltage-source inverters in microgrids based on H∞ and repetitive control. *IEEE Trans. Power Electron.* **2011**, *26*, 943–952. [CrossRef]
20. Zhang, N.; Tang, H.; Yao, C. A systematic method for designing a PR controller and active damping of the LCL filter for single-phase grid-connected PV inverters. *Energies* **2014**, *7*, 3934–3954. [CrossRef]
21. Jeong, H.; Kim, G.; Lee, K. Second-order harmonic reduction technique for photovoltaic power conditioning systems using a proportional-resonant controller. *Energies* **2013**, *6*, 79–96. [CrossRef]
22. Schonardie, M.; Coelho, R.; Schweitzer, R.; Martins, D. Control of the active and reactive power using dq0 transformation in a three-phase grid-connected PV system. In Proceedings of the 2012 IEEE International Symposium Industrial Electronic, Hangzhou, China, 23–26 September 2012; pp. 264–269.
23. Bayo-Salas, A.; Beerten, J.; Rimez, J.; Van Hertem, D. Analysis of control interactions in multi-infeed VSC HVDC connections. *IET Gener. Transm. Distrib.* **2016**, *10*, 1336–1344. [CrossRef]
24. Li, G.-J.; Ruan, S.-Y.; Ooi, B.-T.; Sun, Y.-Z.; Choi, S.S. Autonomous AC grid based on multi-infeed voltage source converter stations. *Electr. Power Compon. Syst.* **2010**, *38*, 558–574. [CrossRef]
25. Kammer, C.; D'Arco, S.; Endegnanew, A.G.; Karimi, A. Convex optimization-based control design for parallel grid-connected inverters. *IEEE Trans. Power Electron.* **2019**, *34*, 6048–6061. [CrossRef]
26. Mahdieh, S.; Qobad, S. Decentralized Multivariable Vector Current Control of Grid-connected Voltage Source Inverters. *IFAC-PapersOnLine* **2020**, *53*, 12410–12415.
27. Jang, M.; Mihai, C.; Agelidis, V.G. A single-phase grid-connected fuel cell system based on a boost-inverter. *IEEE Trans. Power Electron.* **2013**, *28*, 279–288. [CrossRef]
28. Adhikari, S.; Li, F.X. Coordinated V-f and P-Q control of solar photovoltaic generators with MPPT and battery storage in microgrids. *IEEE Trans. Smart Grid* **2014**, *5*, 1270–1281. [CrossRef]
29. Lia, S.; Jaithwaa, I.; Suftaha, R.; Fua, X. Direct-current vector control of three-phase grid-connected converter with L, LC, and LCL filters. *Electr. Power Compon. Syst.* **2015**, *43*, 1644–1655. [CrossRef]
30. Mahlagha, M.; Li, L.; Jianguo, Z. A Model Predictive Control of Parallel Inverters for Distributed Generations in Microgrids. In Proceedings of the IEEE International Conference on Power System Technology (POWERCON), Wollongong, Australia, 28 September–1 October 2016.
31. Zhu, Y.; Zhuo, F.; Shi, H. Accurate Power Sharing Strategy for Complex Microgrid based on Droop Control Method. In Proceedings of the 5th IEEE ECCE Asia Downunder, Melbourne, Australia, 3–6 June 2013.
32. He, J.; Li, Y.W.; Blaabjerg, F. An enhanced islanding microgrid reactive power, imbalance power, and harmonic power sharing scheme. *IEEE Trans. Power Electron.* **2015**, *30*, 3389–3401. [CrossRef]
33. Zhong, Q.C.; Wang, Y.; Ren, B. UDE-based robust droop control of inverters in parallel operation. *IEEE Trans. Ind. Electron.* **2017**, *64*, 7552–7562. [CrossRef]
34. Jasim, M.A.; Jasim, H.B. Grid-Forming and Grid-Following Based Microgrid Inverters Control. *Iraqi J. Electr. Electron. Eng.* **2022**, *18*, 111–131. [CrossRef]
35. Siew-Chong, T.; Yuk-Ming, L.; Chi Kong, T. *Sliding Mode Control of Switching Power Converters Techniques and Implementation*; CRC Press Taylor & Francis Group: Boca Raton, FL, USA, 2011; ISBN 978-1-4398-3025-3.
36. Tan, S.C.; Lai, Y.M.; Tse, C.K.; Cheung, M.K. A Fixed-Frequency Pulsewidth Modulation Based Quasi-Sliding-Mode Controller for Buck Converters. *IEEE Trans. Power Electron.* **2005**, *20*, 1379–1392. [CrossRef]
37. Hanifi, G. Study of Sliding Mode Control of DC-DC Buck Converter. *Energy Power Eng.* **2011**, *3*, 401–406.

38. Vadim, U.; Jurgen, G.; Jingxin, S. *Sliding Mode Control in Electro-Mechanical Systems*, 2nd ed.; CRC Press Taylor & Francis Group: Boca Raton, FL, USA, 2009; ISBN 978-1-4200-6560-2.
39. Zaghba, L.; Borni, A.; Bouchakour, A.; Terki, N. Buck-Boost Converter System Modelling and Incremental Inductance Algorithm for Photovoltaic System via Matlab/Simulink. In Proceedings of the 2nd International Seminar on New and Renewable Energies, Paris, France, 7–8 May 2014; pp. 63–70.
40. Salazar, P.; Ayala, P.; Jiménez, S.G.; Correa, A.F. Design of a Sliding Mode Control for a DC-to-DC Buck-Boost Converter. In Proceedings of the 25th Chinese Control and Decision Conference (CCDC), Guiyang, China, 25–27 May 2013; pp. 4661–4666.
41. Tan, S.C.; Lai, Y.M.; Tse, C.K.; Martinez-Salamero, L. Special family of PWM-based sliding-mode voltage controllers for basic DC–DC converters in discontinuous conduction mode. *IET Electr. Power Appl.* **2007**, *1*, 64–74. [CrossRef]
42. Lai, Y.M.; Tan, S.C.; Wu, C.K. Design of a PWM Based Sliding Mode Controlled Buck-Boost Converter in Continuous Conduction Mode. *ECTI Trans. Electr. Eng. Electron. Commun.* **2007**, *5*, 129–133.
43. Khaild, A.; Hairik, H.A. Static and Dynamic Performances of PWM Based SMCBB Converter: Experimental Investigation. *IOSR J. Electr. Electron. Eng.* **2016**, *11*, 9–18.
44. Khaild, A.; Hairik, H.A. Checking the Robustness of a PWM Sliding Mode Controlled DC/DC Buck-Boost Converter Using its Matlab/Simulink Model. In Proceedings of the 2016 Al-Sadeq International Conference on Multidisciplinary in IT and Communication Science and Applications (AIC-MITCSA), Baghdad, Iraq, 9–10 May 2016.
45. Bilal, N.; Basil, H. A New Coordinated Control of Hybrid Microgrids with Renewable Energy Resources Under Variable Loads and Generation Conditions. *Iraqi J. Electr. Electron. Eng.* **2020**, *16*, 1–20. [CrossRef]
46. Cha, H.; Vu, T.K.; Kim, J.E. Design and Control of Proportional-Resonant Controller Based Photovoltaic Power Conditioning System. In Proceedings of the 2009 IEEE Energy Conversion Congress and Exposition, San Jose, CA, USA, 20–24 September 2009.
47. Shabib, G.; Abd-Elhameed, E.H.; Magdy, G. A New Approach to the Digital Implementation of Analog Controllers for a Power System Control. *Int. J. Sci. Eng. Res.* **2014**, *5*, 419–427.
48. Busarello, T.D.C.; Pomilio, J.A.; Simoes, M.G. Design Procedure for a Digital Proportional-Resonant Current Controller in a Grid Connected Inverter. In Proceedings of the 2018 IEEE 4th Southern Power Electronics Conference (SPEC), Singapore, 10–13 December 2018.
49. Jasim, M.A.; Jawad, M.R.; Ramzy, A.S. Design and Implementation of a Musical Water Fountain Based on Sound Harmonics Using IIR Filters. *Int. J. Comput. Digit. Syst.* **2020**, *9*, 319–333.
50. Alhasnawi, B.N.N.; Jasim, B.H.; Issa, W.; Esteban, M.D. A Novel Cooperative Controller for Inverters of Smart Hybrid AC/DC Microgrids. *Appl. Sci.* **2020**, *10*, 6120. [CrossRef]
51. Stefan, L. Internal Model–Based Control Strategies for Voltage Source Converters. Master's Thesis, Graz University of Technology in Cooperation with Washington State University, Pullman, WA, USA, 2016.